AAAS
Research
Volume 2018, Article ID 6793752, 10 pages
https://doi.org/10.1155/2018/6793752

Research
OFFICIAL JOURNAL OF CAST

Research Article

Topological Nodal States in Circuit Lattice

Kaifa Luo,[1] Rui Yu,[1,*] and Hongming Weng[2,*]

[1]*School of Physics and Technology, Wuhan University, Wuhan 430072, China*
[2]*Beijing National Laboratory for Condensed Matter Physics, Institute of Physics, Chinese Academy of Sciences, Beijing 100190, China*

[*]Correspondence should be addressed to Rui Yu; yurui1983@foxmail.com and Hongming Weng; hmweng@iphy.ac.cn

Received 12 May 2018; Accepted 21 July 2018; Published 2 September 2018

Copyright © 2018 Kaifa Luo et al. Exclusive Licensee Science and Technology Review Publishing House. Distributed under a Creative Commons Attribution License (CC BY 4.0).

The search for artificial structure with tunable topological properties is an interesting research direction of today's topological physics. Here, we introduce a scheme to realize topological nodal states with a three-dimensional periodic inductor-capacitor (LC) circuit lattice, where the topological nodal line state and Weyl state can be achieved by tuning the parameters of inductors and capacitors. A tight-binding-like model is derived to analyze the topological properties of the LC circuit lattice. The key characters of the topological states, such as the drumhead-like surface bands for nodal line state and the Fermi arc-like surface bands for Weyl state, are found in these systems. We also show that the Weyl points are stable with the fabrication errors of electric devices.

1. Introduction

Recently, there is great interest in realizing topological states in various platforms. Topological states, including the quantum Hall states, quantum spin Hall states, Dirac states, Weyl states, and nodal line states, have achieved significant progresses in electronic materials [1–12], cold atoms [13–22], photonics [23–29], phononics [30–36], and mechanical systems [37–47]. In addition, the topological properties in electric circuit system have also been explored in several works [48–53]. The quantum spin Hall-like states have been proposed in two-dimensional circuit lattice via time-reversal symmetric Hofstadter model [48, 49]. The Weyl state has been found in three-dimensional circuit network and proposed to be able to be detected from the boundary resonant signal [51]. The topological Zak phase is discussed in the one-dimensional SSH-type circuit lattice [52]. These proposed electric circuits are composed of interconnected linear lossless passive elements, such as capacitors and inductors. The significant advantages of the circuit lattice are that the parameters of the system are independently artificial adjustable and the symmetry of the lattice is protected by the parameters of electronic components and the way they are connected, rather than their positions in the real space.

From symmetry considerations, three types of nodal line states have been proposed in a great number of literatures [54–56]. Type-A is protected by mirror reflection symmetry [28, 57–61], type-B is protected by the coexistence of time-reversal and space inversion symmetry [20, 21, 59, 62–72], and type-C is protected by the nonsymmorphic space group [73–76]. While the existence of Weyl points does not require any crystalline symmetries except the lattice translational symmetry, Weyl points can only appear when the bands degeneracy is removed by breaking either time-reversal [3, 4] or spacial inversion symmetry [5, 6] as summarized in the review articles [10–12]. In the present work, we demonstrate a feasible strategy to design both nodal line state and Weyl state in a three-dimensional circuit lattice. The nodal line structure we obtained belongs to type-B as discussed above. The Weyl state is achieved by breaking the spacial inversion symmetry. The topological phase transition between them can be controlled by tuning the parameters of the components. In order to investigate their topological properties, we transform the circuit network problem to a tight-binding-like model. Based on the tight-binding model, the novel surface states, including drumhead-like surface bands for nodal line state and Fermi arc-like surface bands for Weyl state, are found in the surface of the circuit lattices. Moreover, the stability of the Weyl points under perturbation of fabrication errors is studied.

2. Results

2.1. Models and Theoretical Framework. The design scheme of realizing the nodal line state and Weyl state in LC circuit lattice is shown below. We consider a honeycomb lattice

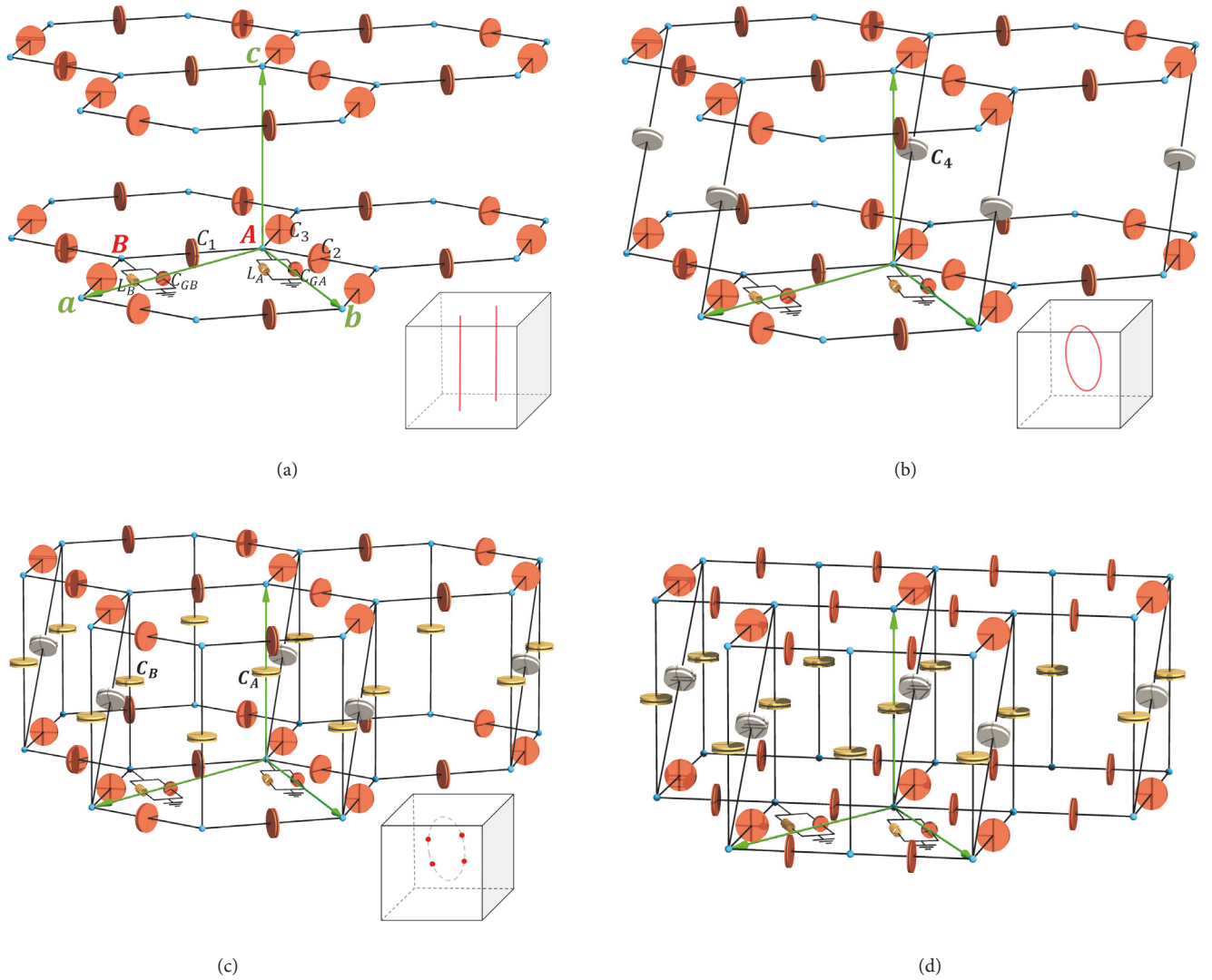


FIGURE 1: Schematic setup of the three-dimensional LC circuit lattice. (a) Honeycomb layers consisting of inductors and capacitors stack along $\boldsymbol{c}$ direction without connection between each layer. The primitive unit cell consists of two inequivalent nodes A and B, which are linked by capacitors C_1, C_2, and C_3 in the $\boldsymbol{a}$-$\boldsymbol{b}$ plane. Each node A (B) is grounded through the parallel connected inductor L_A (L_B) and capacitor C_{GA} (C_{GB}). Lattice vectors are denoted as $\boldsymbol{a}$, $\boldsymbol{b}$, and $\boldsymbol{c}$. The frequency bands structure of the single layer honeycomb LC lattice has two band-crossing points, which are uniform in $\boldsymbol{k}_c$ direction and form two straight nodal lines in the BZ (red colour lines in the inset). (b) Connecting nodes A and nodes B between neighbor-layers with C_4. The nodal lines become $\boldsymbol{k}_c$ dependent and form a closed ring by choosing appropriate C_4. (c) Connecting nodes A-A and nodes B-B between neighbor-layers with C_A and C_B, respectively, and removing the space inversion symmetry by tuning $C_A \neq C_B$ and $C_{GA} \neq C_{GB}$, the nodal ring may be degenerated to Weyl points. The LC lattice can be deformed into (d), which brings convenience for constructing circuit elements in experiments with spectrum topologically invariable.

consisting of capacitors and inductors in $\boldsymbol{a}$-$\boldsymbol{b}$ plane as a starting point. The subnodes A and B are linked by capacitors C_1, C_2, and C_3. Every node A (B) is grounded through the parallel connected inductor L_A (L_B) and capacitor C_{GA} (C_{GB}) as shown in Figure 1(a). Similar to the electronic band structure of graphene, the frequency spectrum of the single layer LC honeycomb lattice contains two band-crossing points in the two-dimensional Brillouin zone (BZ). Stacking the two-dimensional honeycomb lattice along $\boldsymbol{c}$ direction without any coupling between each other, the band-crossing points will form two straight nodal lines in the three-dimensional BZ as shown in Figure 1(a). In order to make the straight nodal lines $\boldsymbol{k}_c$ dependent, we connect nodes A and B between neighbor-layers with C_4 as shown in Figure 1(b). By tuning the value of C_4, these two separate lines are deformed and merged into a closed ring, namely, the nodal line we are searching for. The nodal line structure is protected by the coexistence of time-reversal and space inversion symmetry. If the space inversion symmetry of the circuit system is removed, the continuous nodal line may be degenerated to discrete Weyl points [25]. Following this insight, nodes A-A and B-B between the nearest-neighbor-layers are connected with C_A and C_B, respectively, as shown in Figure 1(c). C_A and C_B and C_{GA} and C_{GB} are deliberately

set to be different, resulting in the space inversion symmetry breaking and emergence of the Weyl points. The LC circuit lattice in Figure 1(c) can be deformed to Figure 1(d). The latter is more convenient to construction of circuit elements in experiments with spectrum topologically invariable. The band structures and the topological properties of the nodal line state and Weyl state for lattice given in Figures 1(b), 1(c), and 1(d) will be detailed in the remain text.

Here, we study the resonance condition of the circuit lattice, where a nonzero distribution of potential satisfies Kirchhoff's law. We follow the method given in Ref. [77], where the periodical circuit lattice problem is transformed into a tight-binding-like model in the momentum space. This approach relies on an analogy between Kirchhoff current equation in periodic circuit lattice and the quantum mechanics with periodic crystalline structure. Therefore, the circuit band structure arises in a manner analogous to electronic band structure in crystals. The tight-binding-like model for the circuit lattice in Figures 1(c) and 1(d) is given as

$$H(\boldsymbol{k})\left|\mathscr{V}(\boldsymbol{k})\right\rangle = \frac{1}{\omega^2 L}\left|\mathscr{V}(\boldsymbol{k})\right\rangle, \tag{1}$$

where

$$H(\boldsymbol{k}) = \sum_{i=0}^{3} d_i(\boldsymbol{k})\,\sigma_i, \tag{2}$$

ω is the resonance frequency of the circuit lattice, matrix $L = \mathrm{diag}(L_A, L_B)$, $\mathscr{V} = (\mathscr{V}_A, \mathscr{V}_B)^T$ is the Bloch states for the potential distributions, and the Pauli matrices are for the space spanned by $(\mathscr{V}_A, \mathscr{V}_B)$. The coefficients in front of the Pauli matrices are given as

$$\begin{aligned} d_0(\boldsymbol{k}) &= C_1 + C_2 + C_3 + C_4 + \frac{(C_{GA} + C_{GB})}{2} \\ &\quad + (C_A + C_B)(1 - \cos k_c), \end{aligned} \tag{3}$$

$$\begin{aligned} d_1(\boldsymbol{k}) &= -C_1 - C_2\cos(k_b - k_a) - C_3\cos k_a \\ &\quad - C_4\cos(k_c - k_a), \end{aligned} \tag{4}$$

$$\begin{aligned} d_2(\boldsymbol{k}) &= C_2\sin(k_b - k_a) - C_3\sin k_a \\ &\quad + C_4\sin(k_c - k_a), \end{aligned} \tag{5}$$

$$d_3(\boldsymbol{k}) = \frac{(C_{GA} - C_{GB})}{2} + (C_A - C_B)(1 - \cos k_c). \tag{6}$$

To simplify the calculations without loss of generality, we set $L_A = L_B = L_G$; therefore the matrix L in (1) is proportional to an identity matrix. Solving (1), we obtain two branches of dispersions $\omega_{1,2}^{-2}(\boldsymbol{k}) = L_G[d_0(\boldsymbol{k}) \pm \sqrt{d_1^2(\boldsymbol{k}) + d_2^2(\boldsymbol{k}) + d_3^2(\boldsymbol{k})}]$ in the BZ. By varying the parameters of capacitor C_is, we can artificially tune the dispersion of $\omega_{1,2}^{-2}(\boldsymbol{k})$ and obtain the desired bands structure. In the following section, we will show that the nodal ring-type and Weyl point-type bands touching points are available in our circuit lattice.

2.2. Nodal Line and Drumhead-Like Surface State. The closed loops of bands crossing points can be protected by the coexistence of space inversion symmetry and time-reversal symmetry [25]. The LC circuit is time-reversal symmetric by nature; we only need to choose a group of parameters of the inductors and capacitors to preserve the space inversion symmetry. For the circuit network given in Figure 1(b), the space inversion symmetry can be obtained by setting $C_{GA} = C_{GB}$, with the inversion center located at the middle point of node A and node B. In this case, $d_3(\boldsymbol{k})$ vanishes ($C_A = C_B = 0$ in Figure 1(b)). The conditions for bands degeneracy require $d_1(\boldsymbol{k}) = 0$ and $d_2(\boldsymbol{k}) = 0$ to be satisfied simultaneously, leading to two restrictions for three variables $\boldsymbol{k} = (k_a, k_b, k_c)$, which gives one-dimensional solution space and forms a continuous nodal ring in the $\boldsymbol{k}$ space. Figure 2(a) illustrates obtained nodal ring structure centered at $Y = (0, \pi, 0)$ point. The band dispersions along Γ-M-A-Y-B-M-Γ are shown in Figure 2(b), where A and B are two nodal points in $k_c = 0$ plane.

The topological properties of a nodal line can be inferred from the winding number $(-1)^{\zeta_1} = (1/\pi)\oint_C \mathscr{A}(\boldsymbol{k})\cdot d\boldsymbol{k}$, where $\mathscr{A}(\boldsymbol{k})$ is the Berry connection and C is a closed loop in the momentum space pierced by the nodal line. $\zeta_1 = 1$ in our model means that the nodal line is topologically stable. Due to the bulk-boundary correspondence, the nontrivial nodal line structure indicates a novel surface state. Based on the tight-binding-like model 2, the surface state in the (001) direction is calculated as shown in Figure 2(c), where a flat surface band nestles inside of the projected node-ring. In order to relate the nontrivial topology induced by the bulk band singularity to edge modes, we calculate the Berry phase of the one-dimensional systems $H_{k_\parallel}(k_c)$ parameterized by the in-plane momentum $k_\parallel = (k_a, k_b)$. The Berry phase for the one-dimensional system is defined as $\theta_{k_\parallel} = \int \mathscr{A}_{k_\parallel} dk_\perp$, where $\mathscr{A}_{k_\parallel}$ is the Berry connection matrix defined as $\mathscr{A}_{k_\parallel} = \langle\mathscr{V}_1|(\boldsymbol{k})\,|\, i\partial_{k_c}|\mathscr{V}_1(\boldsymbol{k})\rangle$. In the one-dimensional parametrized systems, the Berry phase equals π for $k_\parallel$ inside the nodal ring, while it is zero for $k_\parallel$ outside the nodal ring as shown in Figure 2(d).

2.3. Weyl Points and Surface 'Fermi Arc'. Starting with nodal line states, Dirac states or Weyl states are possible to emerge by introducing symmetry breaking terms [25]. Here we show the Weyl states can be realized in the circuit lattice shown in Figures 1(c) and 1(d). The space inversion symmetry of the circuit lattice is easy to be removed by setting $C_{GA} \neq C_{GB}$ and $C_A \neq C_B$. In this case, $d_1(\boldsymbol{k})$ and $d_2(\boldsymbol{k})$ are not affected and the nodal ring structure as solutions of $d_1(\boldsymbol{k}) = d_2(\boldsymbol{k}) = 0$ remains. Now the gap closing condition further requires $d_3(\boldsymbol{k}) = 0$, which leads to $\cos k_c = 1 + (C_{GA} - C_{GB})/2(C_A - C_B)$. Tuning the parameters of C_{GA}, C_{GB}, C_A, and C_B to make the absolute value of the right-hand side of the equation less than 1, $d_3(\boldsymbol{k}) = 0$ determines two planes perpendicular to k_c axis in the first BZ. When these two planes intersect with the nodal ring, as shown in Figure 3(a), there are four crossing points that are the desired Weyl points in the Brillouin zone. Because time-reversal symmetry maps Weyl point at $\boldsymbol{k}$ to $-\boldsymbol{k}$ with the same chirality, to neutralize the chirality in the BZ there must be two other Weyl points with opposite chirality.

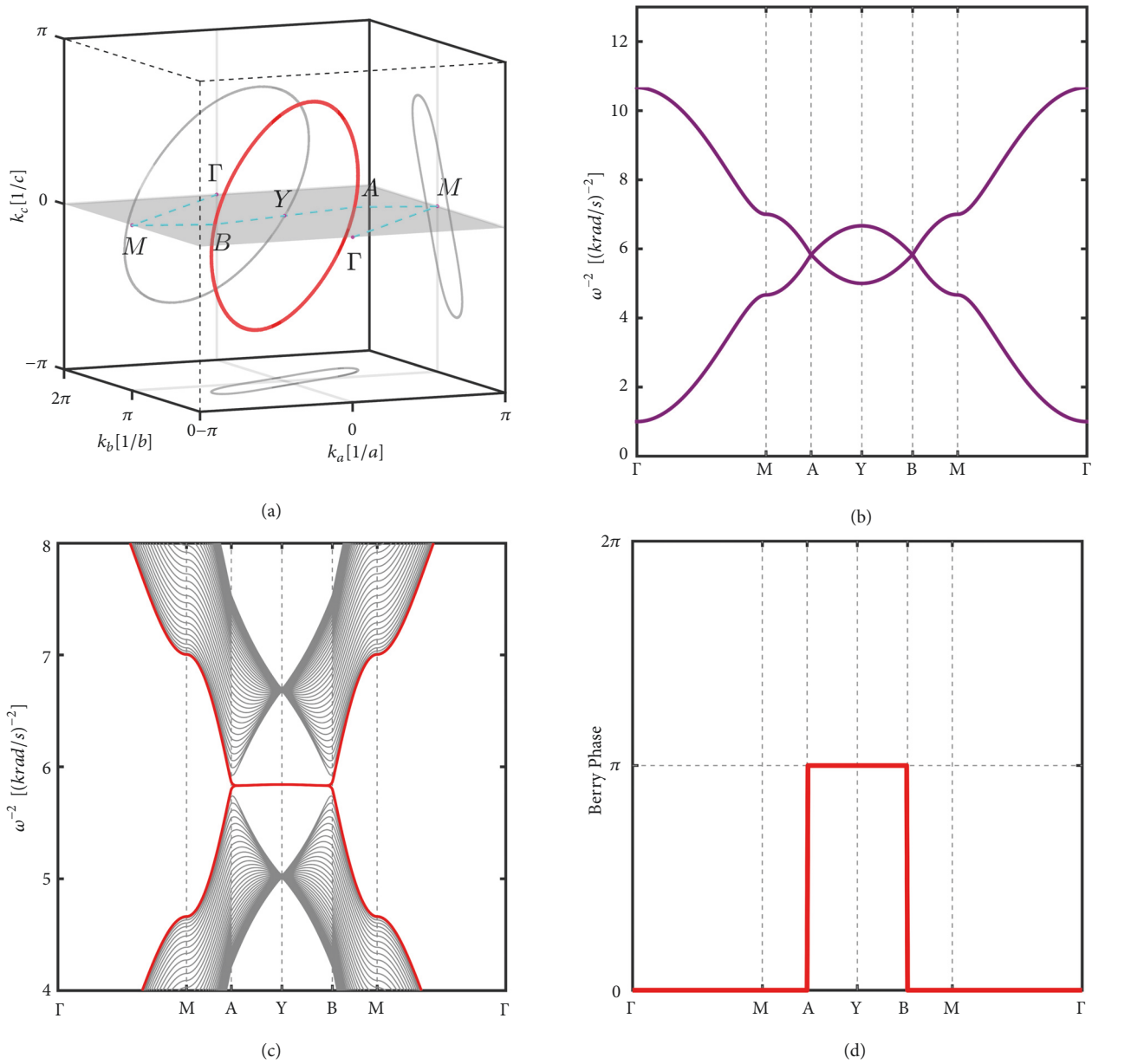


FIGURE 2: (a) Nodal line (in red) in the BZ and its projection on the (001), (010), and (100) planes (in grey). The parameters are set as $C_1 = 1mF$, $C_2 = 2mF$, $C_3 = 1mF$, $C_4 = 0.833mF$, $C_{GA} = C_{GB} = 1mF$, and $L_A = L_B = 1mH$. (b) Band structure along $\Gamma - X - A - B - X - \Gamma$, where A and B are two points with $k_c = 0$ on the nodal line as labeled in (a). (c) The band dispersions with the surface states (red colour lines) on the (001) surface. The drumhead-like surface states are nestled inside the projection of the nodal ring. (d) The Berry phase $\theta_{k_\parallel}$ equals π for $k_\parallel$ inside the nodal ring, while it is zero for $k_\parallel$ outside the nodal ring.

Therefore the minimal number of Weyl points in our circuit lattice has to be four. The chiralities of the Weyl points are determined in the following way. We calculate the Chern number for the lower bulk bands on the planes perpendicular to k_a axis in the 3D BZ. As shown in Figure 3(c), moving along k_a, the increasing (decreasing) of Chern number when the plane passes through the Weyl points indicates that the chiral value of the Weyl points is +1 (−1). The Weyl points with +1 chirality are marked with blue star while red points are for −1 chirality in Figure 3(a).

As a result of the nonzero Chern numbers, topologically protected gapless chiral surface states emerge in the band gap away from the Weyl points. An example of the nontrivial surface band dispersions is shown in Figure 3(b). A surface mode profile at the frequency of the Weyl points is also shown in Figure 3(d). Similar to the Fermi arcs in Weyl semimetals, Weyl pairs with opposite chirality are connected through the segment-like surface dispersion in the surface Brillouin zone. The surface "Fermi arc" for (100) and (010) directions surface can be calculated with the similar method.

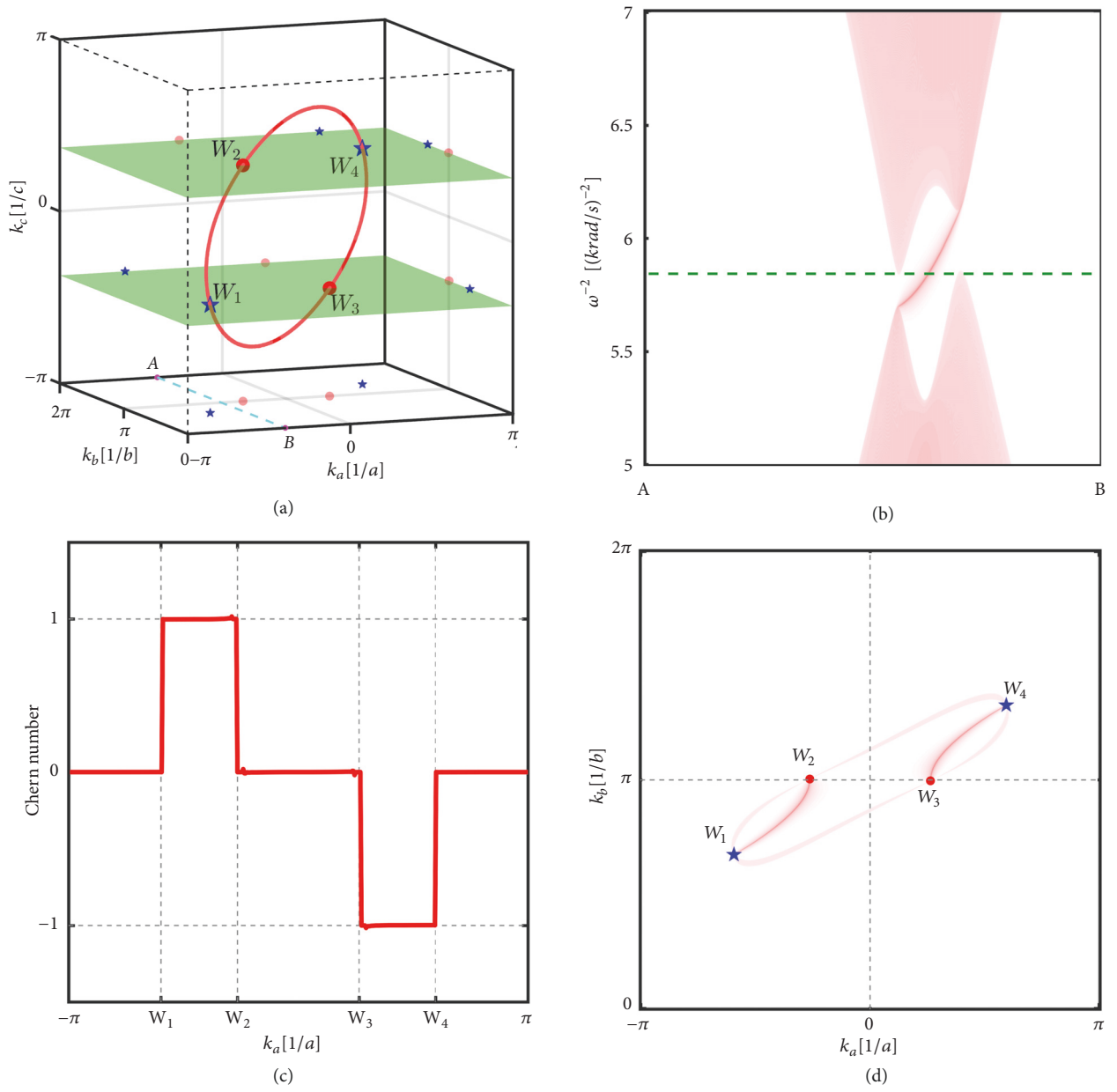


FIGURE 3: (a) Four Weyl points in the Brillouin zone and their projections on (001), (010), and (100) direction. $C_A = 0.2mF$, $C_B = 0.01mF$, and $C_{GA} = 0.77mF$ are used in the calculations. The other parameters are the same as Figure 2. The positions of the Weyl points are the intersection points between the nodal ring determined by $d_1(\boldsymbol{k}) = d_2(\boldsymbol{k}) = 0$ and the two planes determined by $d_3(\boldsymbol{k}) = 0$. The chirality are indicated as blue stars for $\chi = +1$ and red points for $\chi = -1$. (b) The gapless surface band dispersions on the A-B-k_c plane and terminates in the (001) direction. (c) The Chern numbers for the two-dimensional planes perpendicular to k_a. Moving along k_a, the Chern number increases (decreases) when the plane passing through the Weyl points with +1 (−1) chirality. (d) On the (001) surface, Fermi arcs connect the projections of the bulk Weyl nodes of opposite chiralities onto the surface.

2.4. Stability of the Weyl Points. In the above discussions, the inductance and capacitance in the circuit lattice are proposed as a set of precise values, but the fabrication error of the electronic devices brings about certain range of tolerance values. In this paragraph, we discuss whether the fabrication errors influence the results given above. For the nodal line state, maintaining intrinsic space inversion symmetry is a necessary condition. When the fabrication errors are taken into consideration, intrinsic space inversion symmetry is too demanding to preserve; therefore nodal line becomes unstable. However, the existence of the Weyl points does not require extra symmetries except the discrete translation invariant symmetry. It is expected to be more stable than the nodal line state under the perturbation of the fabrication errors. In order to investigate the stability of the Weyl points in the circuit lattice, we employ a 3 × 3 × 3 super cell.

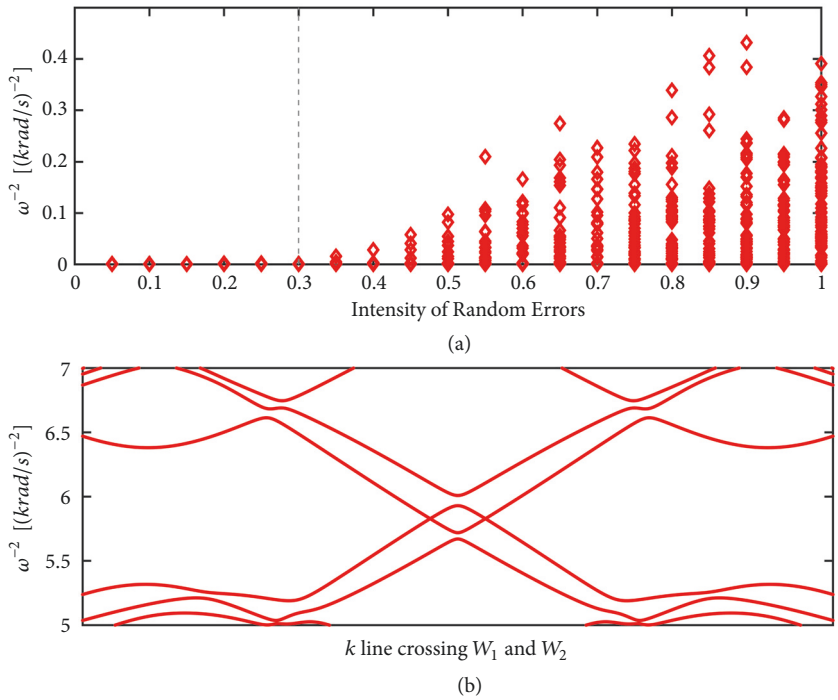


FIGURE 4: (a) The band gap, $\min[\omega_{N/2+1}^{-2} - \omega_{N/2}^{-2}]$ as a function of the tolerance values for a $3 \times 3 \times 3$ super cell. N is number of total bands for the $3 \times 3 \times 3$ super cell. The parameters are the same as Figure 3 without considering the fabrication errors. After taking the fabrication errors into consideration, we repeat 100 times calculations for each tolerance values. The numerical results show that the gap equals zero; i.e., Weyl points exist for the tolerance values less than 30%. Exceeding this value, the gap opens by the fabrication errors. (b) The band dispersions along the $\boldsymbol{k}$ line crossing two Weyl points for a $3 \times 3 \times 3$ super cell with ±20% tolerance values on the capacitors.

In addition, the values of the capacitors' parameters are randomly taken within a certain range around the precise values. In the language of solid state physics, the hopping terms and on-site energies in (6)-(9) are randomly taken. The details are shown in the materials and methods part. To simplify the calculation without loss of key points, we keep L_A and L_B fixed. For each value, we repeat calculations 100 times with different random errors and find the minimal value of the gap between band $N/2+1$ and $N/2$ in each time. Here, N is the number of total bands for the $3\times3\times3$ super cell. As long as these two bands are not gaped, i.e., the gap is zero, the Weyl points still survive. The numerical results in Figure 4(a) show that the Weyl points exist for tolerance values around the precise value less than 30%. Exceeding this tolerance value, the gap opens and we get a topologically trivial circuit. Take a super cell with ±20% tolerance values, for example, we calculate its band structures along the $\boldsymbol{k}$ line crossing two of the gap closing points. The band dispersions in Figure 4(b) show that two bands cross each other and form a pair of Weyl points near $\omega^{-2} = 5.8(krad/s)^{-2}$.

3. Discussion

To summarize, we report that the topological nodal line state and Weyl state can be realized in a three-dimensional classical circuit system. We derived a two-by-two tight-binding-like model to investigate its topological nature. Based on this model, we show that the nodal line structure is protected by the inversion symmetry, which can be achieved by setting $C_{GA} = C_{GB}$ and $C_A = C_B$. When the inversion symmetry is broken, gap opens along the nodal line, while four Weyl points are left in the first BZ. We also confirm that the Weyl state is robust with the fabrication error of the electrical devices. The key characters of the above two topological state, namely, the drumhead-like surface states for nodal line state and 'Fermi arcs' surface state for Weyl state, are conformed by the tight-binding-like model terminated on the (001) direction surface. The topological phase transition between nodal line state and Weyl state can be tuned by changing the parameters of the capacitors and inductors or by controlling the connecting or disconnecting of some elements, for example, the capacitors $C_{A,B}$ and $C_{GA,GB}$ in Figure 1(c), in the circuit lattice. Moreover, in the experimental aspect, the proposed circuit lattice can be manufactured with current technology. The topological properties, such as the patterns for the "Fermi arcs" connecting the Weyl point pairs, can be detected by measuring the potential distribution on the surface of the circuit lattice. This work offers a new, robust platform for realizing and tuning topological nodal line state and Weyl state in the classical system.

4. Materials and Methods

In this section, we present the details of the methods used to calculate the band structure of the circuit lattice. We start with deriving the tight-binding-like model given in (1). The

current I passing through a two-terminal circuit element for a given drop in voltage Δv is described by Ohm's law $I = Y\Delta v$, where Y is admittance. In an alternating current (AC) sinusoidal circuits, the admittance for the ideal inductors and capacitors is $Y_L = 1/j\omega L$ and $Y_C = j\omega C$, respectively. ω is the frequency for the sinusoidal signal and $j = \sqrt{-1}$, following the convention in electric circuits. The currents flow into nodes A and B in the cell located at $\boldsymbol{R} = \boldsymbol{0}$ of circuit lattices given in Figures 1(c) and 1(d) of main text are given as

$$\begin{aligned} I_A(\boldsymbol{0}) = {} & j\omega\left(C_1\left[v_B(\boldsymbol{0}) - v_A(\boldsymbol{0})\right]\right. \\ & + C_2\left[v_B(\boldsymbol{b}-\boldsymbol{a}) - v_A(\boldsymbol{0})\right] + C_3\left[v_B(-\boldsymbol{a}) - v_A(\boldsymbol{0})\right] \\ & + C_4\left[v_B(\boldsymbol{c}-\boldsymbol{a}) - v_A(\boldsymbol{0})\right] + C_A\left[v_A(\boldsymbol{c}) - v_A(\boldsymbol{0})\right] \\ & \left. + C_A\left[v_A(-\boldsymbol{c}) - v_A(\boldsymbol{0})\right] + C_{GA}\left[0 - v_A(\boldsymbol{0})\right]\right) \\ & + \frac{\left[0 - v_A(\boldsymbol{0})\right]}{\left(j\omega L_A\right)} = j\omega\left(C_1 v_B(\boldsymbol{0}) + C_2 v_B(\boldsymbol{b}-\boldsymbol{a})\right. \\ & + C_3 v_B(-\boldsymbol{a}) + C_4 v_B(\boldsymbol{c}-\boldsymbol{a}) + C_A v_A(\boldsymbol{c}) \\ & + C_A v_A(-\boldsymbol{c}) \\ & \left. - \left(C_{GA} + C_1 + C_2 + C_3 + C_4 + 2C_A\right) v_A(\boldsymbol{0})\right) \\ & - \frac{v_A(\boldsymbol{0})}{\left(j\omega L_A\right)}, \end{aligned} \tag{7}$$

and

$$\begin{aligned} I_B(\boldsymbol{0}) = {} & j\omega\left(C_1\left[v_A(\boldsymbol{0}) - v_B(\boldsymbol{0})\right]\right. \\ & + C_2\left[v_A(\boldsymbol{a}-\boldsymbol{b}) - v_B(\boldsymbol{0})\right] + C_3\left[v_A(\boldsymbol{a}) - v_B(\boldsymbol{0})\right] \\ & + C_4\left[v_A(\boldsymbol{a}-\boldsymbol{c}) - v_B(\boldsymbol{0})\right] + C_B\left[v_B(\boldsymbol{c}) - v_B(\boldsymbol{0})\right] \\ & \left. + C_B\left[v_B(-\boldsymbol{c}) - v_B(\boldsymbol{0})\right] + C_{GB}\left[0 - v_B(\boldsymbol{0})\right]\right) \\ & + \frac{\left[0 - v_B(\boldsymbol{0})\right]}{\left(j\omega L_B\right)} = j\omega\left(C_1 v_A(\boldsymbol{0}) + C_2 v_A(\boldsymbol{a}-\boldsymbol{b})\right. \\ & + C_3 v_A(\boldsymbol{a}) + C_4 v_A(\boldsymbol{a}-\boldsymbol{c}) + C_B v_B(-\boldsymbol{c}) + C_B v_B(\boldsymbol{c}) \\ & \left. - \left(C_{GB} + C_1 + C_2 + C_3 + C_4 + 2C_B\right) v_B(\boldsymbol{0})\right) \\ & - \frac{v_B(\boldsymbol{0})}{\left(j\omega L_B\right)}. \end{aligned} \tag{8}$$

Kirchhoff's current law demands that $I_A(\boldsymbol{0})$ and $I_B(\boldsymbol{0})$ are zero. Dividing $j\omega$ on both sides of (7) and (8), we get

$$\begin{aligned} & -\left(C_1 v_B(\boldsymbol{0}) + C_2 v_B(\boldsymbol{b}-\boldsymbol{a}) + C_3 v_B(-\boldsymbol{a})\right. \\ & \quad + C_4 v_B(\boldsymbol{c}-\boldsymbol{a}) + C_A v_A(\boldsymbol{c}) + C_A v_A(-\boldsymbol{c}) \\ & \quad \left. - \left(C_{GA} + C_1 + C_2 + C_3 + C_4 + 2C_A\right) v_A(\boldsymbol{0})\right) \\ & \quad = \frac{1}{\omega^2 L_A} v_A(\boldsymbol{0}), \end{aligned} \tag{9}$$

$$\begin{aligned} & -\left(C_1 v_A(\boldsymbol{0}) + C_2 v_A(\boldsymbol{a}-\boldsymbol{b}) + C_3 v_A(-\boldsymbol{b})\right. \\ & \quad + C_4 v_A(\boldsymbol{a}-\boldsymbol{c}) + C_B v_B(-\boldsymbol{c}) + C_B v_B(\boldsymbol{c}) \\ & \quad \left. - \left(C_{GB} + C_1 + C_2 + C_3 + C_4 + 2C_B\right) v_B(\boldsymbol{0})\right) \\ & \quad = \frac{1}{\omega^2 L_B} v_B(\boldsymbol{0}). \end{aligned} \tag{10}$$

With the similar method, we can obtain the equations for the potential distribution $v_A(\boldsymbol{R})$ and $v_B(\boldsymbol{R})$ on the whole lattice. Writing these equations in a matrix form, we have

$$YV = \frac{1}{\omega^2 L} V, \tag{11}$$

where V is a vector for the potential distribution on A and B nodes of the circuit lattice, L is a diagonal matrix composed of L_A and L_B, and Y is the admittance matrix containing all information of the involving capacitors in our circuit. Equation (11) is an eigenvalue problem, in which V is the wave function and $1/\omega^2 L$ is the eigenvalue. Following this insight, the admittance matrix Y can be interpreted as tight-binding Hamiltonian in real space. Hopping terms and on-site energies of the tight-binding model can be extracted from (9) and (10), which are listed below:

$$\begin{aligned} H_{AB}(\boldsymbol{R} = \boldsymbol{0}) &= -C_1; \\ H_{AB}(\boldsymbol{R} = \boldsymbol{b}-\boldsymbol{a}) &= -C_2; \\ H_{AB}(\boldsymbol{R} = -\boldsymbol{a}) &= -C_3; \\ H_{AB}(\boldsymbol{R} = \boldsymbol{c}-\boldsymbol{a}) &= -C_4; \end{aligned} \tag{12}$$

$$\begin{aligned} H_{AA}(\boldsymbol{R} = \pm\boldsymbol{c}) &= -C_A; \\ H_{BB}(\boldsymbol{R} = \pm\boldsymbol{c}) &= -C_B; \end{aligned} \tag{13}$$

$$H_{AA}(\boldsymbol{R} = \boldsymbol{0}) = C_{GA} + C_1 + C_2 + C_3 + C_4 + 2C_A; \tag{14}$$

$$H_{BB}(\boldsymbol{R} = \boldsymbol{0}) = C_{GB} + C_1 + C_2 + C_3 + C_4 + 2C_B, \tag{15}$$

where $\boldsymbol{R}$ is the lattice vector and $H_{mn}(\boldsymbol{R})$ are the tight-binding parameters between node m located at the home unit cell and node n located at $\boldsymbol{R}$. With these terms, the tight-bind Hamiltonian in the momentum $\boldsymbol{k}$ space can be obtained through Fourier transformation $H_{mn}(\boldsymbol{k}) = \sum_{\boldsymbol{R}} e^{i\boldsymbol{k}\cdot\boldsymbol{R}} H_{mn}(\boldsymbol{R})$. The elements of the Hamiltonian are given as

$$\begin{aligned} H_{AA}(\boldsymbol{k}) = {} & C_{GA} + C_1 + C_2 + C_3 + C_4 + 2C_A \\ & - C_A\left(e^{ik_c} + e^{-ik_c}\right), \end{aligned} \tag{16}$$

$$\begin{aligned} H_{BB}(\boldsymbol{k}) = {} & C_{GB} + C_1 + C_2 + C_3 + C_4 + 2C_B \\ & - C_B\left(e^{ik_c} + e^{-ik_c}\right), \end{aligned} \tag{17}$$

$$H_{AB}(\boldsymbol{k}) = -C_1 - C_2 e^{i(k_b - k_a)} - C_3 e^{-ik_a} - C_4 e^{i(k_c - k_a)}, \tag{18}$$

with the Bloch-like basis function $|\mathscr{V}_m(\boldsymbol{k})\rangle = \sum_{\boldsymbol{R}} e^{i\boldsymbol{k}\cdot\boldsymbol{R}}|v_m(\boldsymbol{R})\rangle$, $m = A, B$. Rewriting the 2 by 2 Hamiltonian matrix with the help of Pauli matrices, we get

$$H(\boldsymbol{k}) = \sum_{i=0}^{3} d_i(\boldsymbol{k})\,\sigma_i \tag{19}$$

with

$$\begin{aligned} d_0(\boldsymbol{k}) &= C_1 + C_2 + C_3 + C_4 + \frac{(C_{GA} + C_{GB})}{2} \\ &\quad + (C_A + C_B)(1 - \cos k_c), \end{aligned} \tag{20}$$

$$\begin{aligned} d_1(\boldsymbol{k}) &= -C_1 - C_2\cos(k_b - k_a) - C_3\cos k_a \\ &\quad - C_4\cos(k_c - k_a), \end{aligned} \tag{21}$$

$$\begin{aligned} d_2(\boldsymbol{k}) &= C_2\sin(k_b - k_a) - C_3\sin k_a \\ &\quad + C_4\sin(k_c - k_a), \end{aligned} \tag{22}$$

$$d_3(\boldsymbol{k}) = \frac{(C_{GA} - C_{GB})}{2} + (C_A - C_B)(1 - \cos k_c), \tag{23}$$

which is the tight-binding-like model given in (2).

For the single layer honeycomb circuit lattice given in Figure 1(a), C_4, C_A, and C_B vanish. If we set $C_{GA} = C_{GB}$, we have

$$d_1(\boldsymbol{k}) = -C_1 - C_2\cos(k_b - k_a) - C_3\cos k_a, \tag{24}$$

$$d_2(\boldsymbol{k}) = C_2\sin(k_b - k_a) - C_3\sin k_a, \tag{25}$$

and

$$d_3(\boldsymbol{k}) = 0. \tag{26}$$

The appearance of gap closing points requires $d_1(\boldsymbol{k}) = d_2(\boldsymbol{k}) = 0$, which lead to

$$C_1 + C_2 e^{-i(k_a - k_b)} + C_3 e^{-ik_a} = 0. \tag{27}$$

As long as the three values of C_1, C_2, and C_3 satisfy the triangle inequality theorem, two band-crossing points can be found in the k_a-k_b plane.

Conflicts of Interest

The authors declare that they have no financial conflicts of interest.

Authors' Contributions

Rui Yu conceived the research. Rui Yu, Kaifa Luo, and Hongming Weng performed the theoretical analysis and the calculations. All authors contributed to the manuscript writing.

Acknowledgments

The authors thank Hua Jiang, Yuanyuan Zhao, and Ang Cao for their very helpful discussions. This work was supported by the National Key Research and Development Program of China (nos. 2017YFA0303402, 2017YFA0304700, and 2016YFA0300600) and the National Natural Science Foundation of China (nos. 11674077, 11422428, 11674369, and 11404024). Rui Yu acknowledges funding from the National Thousand Young Talents Program. The numerical calculations in this work have been done on the supercomputing system in the Supercomputing Center of Wuhan University.

References

[1] M. Z. Hasan and C. L. Kane, "Colloquium: topological insulators," *Reviews of Modern Physics*, vol. 82, no. 4, pp. 3045–3067, 2010.

[2] X.-L. Qi and S.-C. Zhang, "Topological insulators and superconductors," *Reviews of Modern Physics*, vol. 83, no. 4, pp. 1057–1110, 2011.

[3] X. Wan, A. M. Turner, A. Vishwanath, and S. Y. Savrasov, "Topological semimetal and Fermi-arc surface states in the electronic structure of pyrochlore iridates," *Physical Review B: Condensed Matter and Materials Physics*, vol. 83, no. 20, 2011.

[4] G. Xu, H. Weng, Z. Wang, X. Dai, and Z. Fang, "Chern semimetal and the quantized anomalous Hall effect in HgCr 2Se4," *Physical Review Letters*, vol. 107, no. 18, 2011.

[5] H. Weng, C. Fang, Z. Fang, B. Andrei Bernevig, and X. Dai, "Weyl semimetal phase in noncentrosymmetric transition-metal monophosphides," *Physical Review X*, vol. 5, no. 1, 2015.

[6] S.-M. Huang, S.-Y. Xu, I. Belopolski et al., "A Weyl Fermion semimetal with surface Fermi arcs in the transition metal monopnictide TaAs class," *Nature Communications*, vol. 6, 2015.

[7] H. Weng, R. Yu, X. Hu, X. Dai, and Z. Fang, "Quantum anomalous Hall effect and related topological electronic states," *Advances in Physics*, vol. 64, no. 3, pp. 227–282, 2015.

[8] B. Lv, H. Weng, B. Fu et al., "Experimental Discovery of Weyl Semimetal TaAs," *Physical Review X*, vol. 5, no. 3, 2015.

[9] S.-Y. Xu, I. Belopolski, N. Alidoust et al., "Discovery of a Weyl fermion semimetal and topological Fermi arcs," *Science*, vol. 349, no. 6248, pp. 613–617, 2015.

[10] H. Weng, X. Dai, and Z. Fang, "Topological semimetals predicted from first-principles calculations," *Journal of Physics: Condensed Matter*, vol. 28, no. 30, p. 303001, 2016.

[11] N. P. Armitage, E. J. Mele, and A. Vishwanath, "Weyl and Dirac semimetals in three-dimensional solids," *Reviews of Modern Physics*, vol. 90, no. 1, 015001, 57 pages, 2018.

[12] A. Burkov, "Weyl metals," *Annual Review of Condensed Matter Physics*, vol. 9, pp. 359–378, 2018.

[13] N. Goldman, I. Satija, P. Nikolic et al., "Realistic time-reversal invariant topological insulators with neutral atoms," *Physical Review Letters*, vol. 105, no. 25, 2010.

[14] K. Sun, W. V. Liu, A. Hemmerich, and S. Das Sarma, "Topological semimetal in a fermionic optical lattice," *Nature Physics*, vol. 8, no. 1, pp. 67–70, 2012.

[15] G. Jotzu, M. Messer, R. Desbuquois et al., "Experimental realization of the topological Haldane model with ultracold fermions," *Nature*, vol. 515, no. 7526, pp. 237–240, 2014.

[16] M. Aidelsburger, M. Lohse, C. Schweizer et al., "Measuring the Chern number of Hofstadter bands with ultracold bosonic atoms," *Nature Physics*, vol. 11, no. 2, pp. 162–166, 2015.

[17] Y. Xu, F. Zhang, and C. Zhang, "Structured Weyl points in spin-orbit coupled fermionic superfluids," *Physical Review Letters*, vol. 115, no. 26, 2015.

[18] T. Dubček, C. J. Kennedy, L. Lu, W. Ketterle, M. Soljačić, and H. Buljan, "Weyl points in three-dimensional optical lattices: synthetic magnetic monopoles in momentum space," *Physical Review Letters*, vol. 114, no. 22, Article ID 225301, 2015.

[19] D. Zhang, S. Zhu, and Z. D. Wang, "Simulating and exploring Weyl semimetal physics with cold atoms in a two-dimensional optical lattice," *Physical Review A: Atomic, Molecular and Optical Physics*, vol. 92, no. 1, 2015.

[20] W. Chen, H. Lu, and J. Hou, "Topological semimetals with a double-helix nodal link," *Physical Review B: Condensed Matter and Materials Physics*, vol. 96, no. 4, 2017.

[21] R. Bi, Z. Yan, L. Lu, and Z. Wang, "Nodal-knot semimetals," *Physical Review B: Condensed Matter and Materials Physics*, vol. 96, no. 20, 2017.

[22] X. Mai, D. Zhang, Z. Li, and S. Zhu, "Exploring topological double-Weyl semimetals with cold atoms in optical lattices," *Physical Review A: Atomic, Molecular and Optical Physics*, vol. 95, no. 6, 2017.

[23] S. Raghu and F. D. M. Haldane, "Analogs of quantum-Hall-effect edge states in photonic crystals," *Physical Review A: Atomic, Molecular and Optical Physics*, vol. 78, Article ID 033834, 2008.

[24] F. D. M. Haldane and S. Raghu, "Possible realization of directional optical waveguides in photonic crystals with broken time-reversal symmetry," *Physical Review Letters*, vol. 100, no. 1, Article ID 013904, 4 pages, 2008.

[25] L. Lu, L. Fu, J. D. Joannopoulos, and M. Soljacic, "Weyl points and line nodes in gyroid photonic crystals," *Nature Photonics*, vol. 7, no. 4, pp. 294–299, 2013.

[26] L. Lu, J. D. Joannopoulos, and M. Soljačić, "Topological photonics," *Nature Photonics*, vol. 8, no. 11, pp. 821–829, 2014.

[27] M. C. Rechtsman, J. M. Zeuner, Y. Plotnik et al., "Photonic Floquet topological insulators," *Nature*, vol. 496, no. 7444, pp. 196–200, 2013.

[28] Q. Yan, R. Liu, Z. Yan et al., "Experimental discovery of nodal chains," *Nature Physics*, vol. 14, no. 5, pp. 461–464, 2018.

[29] T. Ozawa, H. M. Price, A. Amo et al., "Topological Photonics," arXiv: 1802.04173, 2018.

[30] E. Prodan and C. Prodan, "Topological phonon modes and their role in dynamic instability of microtubules," *Physical Review Letters*, vol. 103, no. 24, 2009.

[31] N. Berg, K. Joel, M. Koolyk, and E. Prodan, "Topological phonon modes in filamentary structures," *Physical Review E: Statistical, Nonlinear, and Soft Matter Physics*, vol. 83, no. 2, 2011.

[32] P. Wang, L. Lu, and K. Bertoldi, "Topological phononic crystals with one-way elastic edge waves," *Physical Review Letters*, vol. 115, no. 10, 2015.

[33] H. C. Po, Y. Bahri, and A. Vishwanath, "Phonon analog of topological nodal semimetals," *Physical Review B: Condensed Matter and Materials Physics*, vol. 93, no. 20, 2016.

[34] Y. Xiao, G. Ma, Z. Zhang, and C. Chan, "Topological subspace-induced bound state in the continuum," *Physical Review Letters*, vol. 118, no. 16, 2017.

[35] F. Li, X. Huang, J. Lu, J. Ma, and Z. Liu, "Weyl points and Fermi arcs in a chiral phononic crystal," *Nature Physics*, vol. 14, no. 1, pp. 30–34, 2017.

[36] T. Zhang, Z. Song, A. Alexandradinata et al., "Double-Weyl phonons in transition-metal monosilicides," *Physical Review Letters*, vol. 120, Article ID 016401, 2018.

[37] C. L. Kane and T. C. Lubensky, "Topological boundary modes in isostatic lattices," *Nature Physics*, vol. 10, no. 1, pp. 39–45, 2013.

[38] B. G. Chen, N. Upadhyaya, and V. Vitelli, "Nonlinear conduction via solitons in a topological mechanical insulator," *Proceedings of the National Acadamy of Sciences of the United States of America*, vol. 111, no. 36, pp. 13004–13009, 2014.

[39] S. Roman and D. H. Sebastian, "Observation of phononic helical edge states in a mechanical topological insulator," *Science*, vol. 349, no. 6243, pp. 47–50, 2015.

[40] L. M. Nash, D. Kleckner, A. Read, V. Vitelli, A. M. Turner, and W. T. M. Irvine, "Topological mechanics of gyroscopic metamaterials," in *Proceedings of the National Acadamy of Sciences of the United States of America*, vol. 112, pp. 14495–14500, 2015.

[41] J. Paulose, B. G.-G. Chen, and V. Vitelli, "Topological modes bound to dislocations in mechanical metamaterials," *Nature Physics*, vol. 11, no. 2, pp. 153–156, 2015.

[42] T. Kariyado and Y. Hatsugai, "Manipulation of dirac cones in mechanical graphene," *Scientific Reports*, vol. 5, 2015.

[43] A. S. Meeussen, J. Paulose, and V. Vitelli, "Geared topological metamaterials with tunable mechanical stability," *Physical Review X*, vol. 6, no. 4, 2016.

[44] B. P. Abbott, R. Abbott, and T. D. Abbott, "Observation of gravitational waves from a binary black hole merger," *Physical Review Letters*, vol. 116, Article ID 061102, 2016.

[45] R. Süsstrunk and S. D. Huber, "Classification of topological phonons in linear mechanical metamaterials," *Proceedings of the National Acadamy of Sciences of the United States of America*, vol. 113, no. 33, pp. E4767–E4775, 2016.

[46] C. Coulais, D. Sounas, and A. Alù, "Static non-reciprocity in mechanical metamaterials," *Nature*, vol. 542, no. 7642, pp. 461–464, 2017.

[47] Z. Xiong, H. Wang, H. Ge et al., "Topological node lines in mechanical metacrystals," *Physical Review B: Condensed Matter and Materials Physics*, vol. 97, no. 18, 2018.

[48] J. Ningyuan, C. Owens, A. Sommer, D. Schuster, and J. Simon, "Time- and site-resolved dynamics in a topological circuit," *Physical Review X*, vol. 5, no. 2, 2015.

[49] V. V. Albert, L. I. Glazman, and L. Jiang, "Topological properties of linear circuit lattices," *Physical Review Letters*, vol. 114, no. 17, Article ID 173902, 6 pages, 2015.

[50] M. Tymchenko and A. Alù, "Circuit-based magnetless floquet topological insulator," in *Proceedings of the 10th International Congress on Advanced Electromagnetic Materials in Microwaves and Optics, METAMATERIALS 2016*, pp. 373–375, Greece, September 2016.

[51] C. H. Lee, S. Imhof, C. Berger et al., "Topolectrical circuits," *Communications Physics*, vol. 1, no. 1, 2018.

[52] T. Goren, K. Plekhanov, F. Appas, and K. Le Hur, "Topological Zak phase in strongly coupled LC circuits," *Physical Review B: Condensed Matter and Materials Physics*, vol. 97, no. 4, 2018.

[53] Y. Li, Y. Sun, W. Zhu et al., "Generating electromagnetic modes with fine tunable orbital angular momentum by planar topological circuits," arXiv:1801.04395, 2018.

[54] C. Fang, H. Weng, X. Dai, and Z. Fang, "Topological nodal line semimetals," *Chinese Physics B*, vol. 25, no. 11, p. 117106, 2016.

[55] R. Yu, Z. Fang, X. Dai, and H. Weng, "Topological nodal line semimetals predicted from first-principles calculations," *Frontiers of Physics*, vol. 12, no. 3, 2017.

[56] S.-Y. Yang, H. Yang, E. Derunova, S. S. Parkin, B. Yan, and M. N. Ali, "Symmetry demanded topological nodal-line materials," in *Advances in Physics: X*, vol. 3, 2018.

[57] C. Chiu and A. P. Schnyder, "Classification of reflection-symmetry-protected topological semimetals and nodal superconductors," *Physical Review B: Condensed Matter and Materials Physics*, vol. 90, no. 20, 2014.

[58] G. Bian, T.-R. Chang, R. Sankar et al., "Topological nodal-line fermions in spin-orbit metal PbTaSe2," *Nature Communications*, vol. 7, 2016.

[59] R. Li, H. Ma, X. Cheng et al., "Dirac node lines in pure alkali earth metals," *Physical Review Letters*, vol. 117, no. 9, 2016.

[60] A. Yamakage, Y. Yamakawa, Y. Tanaka, and Y. Okamoto, "Line-node Dirac semimetal and topological insulating phase in noncentrosymmetric pnictides CaAgX (X = P, As)," *Journal of the Physical Society of Japan*, vol. 85, no. 1, 2016.

[61] G. Bian, T.-R. Chang, H. Zheng et al., "Drumhead surface states and topological nodal-line fermions in TlTaSe2," *Physical Review B: Condensed Matter and Materials Physics*, vol. 93, no. 12, 2016.

[62] H. Weng, Y. Liang, Q. Xu et al., "Topological node-line semimetal in three-dimensional graphene networks," *Physical Review B*, vol. 92, Article ID 045108, 2015.

[63] Y. Kim, B. J. Wieder, C. Kane, and A. M. Rappe, "Dirac line nodes in inversion-symmetric crystals," *Physical Review Letters*, vol. 115, no. 3, 2015.

[64] R. Yu, H. Weng, Z. Fang, X. Dai, and X. Hu, "Topological node-line semimetal and dirac semimetal state in antiperovskite," *Physical Review Letters*, vol. 115, no. 3, 2015.

[65] L. S. Xie, L. M. Schoop, E. M. Seibel, Q. D. Gibson, W. Xie, and R. J. Cava, "A new form of Ca3P2 with a ring of Dirac nodes," *APL Materials*, vol. 3, no. 8, 2015.

[66] F. J. Gómez-Ruiz, J. J. Mendoza-Arenas, F. J. Rodríguez, C. Tejedor, and L. Quiroga, "Quantum phase transitions detected by a local probe using time correlations and violations of Leggett-Garg inequalities," *Physical Review B: Condensed Matter and Materials Physics*, vol. 93, no. 3, Article ID 035441, 2016.

[67] M. Zeng, C. Fang, G. Chang et al., "Topological semimetals and topological insulators in rare earth monopnictides," 2015, https://arxiv.org/abs/1504.03492.

[68] M. Hirayama, R. Okugawa, T. Miyake, and S. Murakami, "Topological Dirac nodal lines and surface charges in fcc alkaline earth metals," *Nature Communications*, vol. 8, 2017.

[69] Y. Chen, Y. Xie, S. A. Yang et al., "Nanostructured carbon allotropes with Weyl-like loops and points," *Nano Letters*, vol. 15, no. 10, pp. 6974–6978, 2015.

[70] H. Huang, J. Liu, D. Vanderbilt, and W. Duan, "Topological nodal-line semimetals in alkaline-earth stannides, germanides, and silicides," *Physical Review B: Condensed Matter and Materials Physics*, vol. 93, no. 20, 2016.

[71] Y. Du, F. Tang, D. Wang et al., "CaTe: a new topological node-line and Dirac semimetal," *npj Quantum Materials*, vol. 2, no. 1, 2017.

[72] Q. Xu, R. Yu, Z. Fang, X. Dai, and H. Weng, "Topological nodal line semimetals in the CaP3 family of materials," *Physical Review B: Condensed Matter and Materials Physics*, vol. 95, Article ID 045136, 2017.

[73] C. Fang, Y. Chen, H. Kee, and L. Fu, "Topological nodal line semimetals with and without spin-orbital coupling," *Physical Review B: Condensed Matter and Materials Physics*, vol. 92, no. 8, 2015.

[74] T. Bzdušek, Q. Wu, A. Rüegg, M. Sigrist, and A. A. Soluyanov, "Nodal-chain metals," *Nature*, vol. 538, no. 7623, pp. 75–78, 2016.

[75] Q. Liang, J. Zhou, R. Yu, Z. Wang, and H. Weng, "Node-surface and node-line fermions from nonsymmorphic lattice symmetries," *Physical Review B: Condensed Matter and Materials Physics*, vol. 93, no. 8, 2016.

[76] S. Li, Y. Liu, S. Wang et al., " Nonsymmorphic-symmetry-protected hourglass Dirac loop, nodal line, and Dirac point in bulk and monolayer ," *Physical Review B: Condensed Matter and Materials Physics*, vol. 97, no. 4, 2018.

[77] Y. Nakata, T. Okada, T. Nakanishi, and M. Kitano, "Circuit model for hybridization modes in metamaterials and its analogy to the quantum tight-binding model," *Physica Status Solidi (b) – Basic Solid State Physics*, vol. 249, no. 11, pp. 2293–2302, 2012.